SCIENCE CHINA
Information Sciences

• RESEARCH PAPER •

June 2016, Vol. 59 062310:1–062310:15
doi: 10.1007/s11432-015-5477-5

DLSLA 3-D SAR imaging algorithm for off-grid targets based on pseudo-polar formatting and atomic norm minimization

Qian BAO[1,2]*, Kuoye HAN[3], Xueming PENG[4], Wen HONG[1], Bingchen ZHANG[1] & Weixian TAN[5]

[1]*Science and Technology on Microwave Imaging Laboratory (MITL), Institute of Electronics, Chinese Academy of Sciences (IECAS), Beijing* 100190*, China;*
[2]*School of Electronic and Communication Engineering, University of Chinese Academy of Sciences (UCAS), Beijing* 100190*, China;*
[3]*Information System Technology Institute, Information Science Academy of China Electronics Technology Group Corporation, Beijing* 100086*, China;*
[4]*Global RD Centre (Shanghai), Carestream Health Incorporated, Shanghai* 200090*, China;*
[5]*College of Information Engineering, Inner Mongolia University of Technology, Hohhot* 010051*, China*

Received September 7, 2015; accepted October 20, 2015; published online April 23, 2016

Abstract This paper concerns the imaging problem for downward looking sparse linear array three-dimensional synthetic aperture radar (DLSLA 3-D SAR) under the circumstance of sparse and non-uniform cross-track dimensional virtual phase centers configuration. Since the 3-D imaging scene behaves typical sparsity in a certain domain, sparse recovery approaches hold the potential to achieve a better reconstruction performance. However, most of the existing compressive sensing (CS) algorithms assume the scatterers located on the pre-discretized grids, which is often violated by the off-grid effect. By contrast, atomic norm minimization (ANM) deals with sparse recovery problem directly on continuous space instead of discrete grids. This paper firstly analyzes the off-grid effect in DLSLA 3-D SAR sparse image reconstruction, and then introduces an imaging method applied to off-gird targets reconstruction which combines 3-D pseudo-polar formatting algorithm (pseudo-PFA) with ANM. With the proposed method, wave propagation and along-track image reconstruction are operated with pseudo-PFA, then the cross-track reconstruction is implemented with semidefinite programming (SDP) based on the ANM model. The proposed method holds the advantage of avoiding the off-grid effect and managing to locate the off-grid targets to accurate locations in different imaging scenes. The performance of the proposed method is verified and evaluated by the 3-D image reconstruction of different scenes, i.e., point targets and distributed scene.

Keywords atomic norm minimization, DLSLA 3-D SAR, sparse recovery, off-grid targets, pseudo-PFA, 3-D imaging

Citation Bao Q, Han K Y, Peng X M, et al. DLSLA 3-D SAR imaging algorithm for off-grid targets based on pseudo-polar formatting and atomic norm minimization. Sci China Inf Sci, 2016, 59(6): 062310, doi: 10.1007/s11432-015-5477-5

* Corresponding author (email: baoqiancherry@163.com)

1 Introduction

Three-dimensional synthetic aperture radar (3-D SAR) is a new development of traditional 2-D SAR which often suffers from distortions such as layover, shadowing and foreshortening [1]. Compared with any other 3-D SAR, e.g., TomoSAR [2, 3] or CSAR [4], whose trajectory is hard to control accurately, downward looking sparse linear array 3-D SAR (DLSLA 3-D SAR) puts less stress on trajectory control and works in a more flexible mode. DLSLA 3-D SAR observes the nadir areas of the platform and can obtain the true 3-D scene scatterers distribution and scattering properties, i.e., the 3-D resolution, by pulse compression in wave propagation dimension, along-track aperture synthesis by platform movement, and cross-track aperture synthesis with physical sparse linear array [5–12].

In recent years, DLSLA 3-D SAR imaging methods have attracted lots of attention. Most of the proposed methods, such as 3-D range migration algorithm [6], 3-D pseudo-PFA [7], are all established on the assumption that the sparse linear array can achieve uniform virtual antenna phase centers (APC) like that in the ARTINO system [8]. However, in practical system, the APCs distribution is usually non-uniform and sparse [9] due to some inevitable factors, e.g., installation restriction, wing vibration, etc., which will make the above-mentioned cross-track dimensional Fourier-based methods ineffective.

For DLSLA 3-D SAR with sparse and non-uniform APCs distribution, there are two main imaging methods: time-domain correlation (TDC) which suffers from low computational efficiency and high sidelobes [1, 5], and compressive sensing (CS) methods [9–11]. CS-based methods enable the reconstruction of sparse or compressible signal using a much smaller number of samples than that under the Nyquist criterion [13]. Since the 3-D observed scene behaves typical sparsity in a certain domain, CS methods have been successfully applied to 3-D SAR imaging [2, 3]. For DLSLA 3-D SAR imaging, in [5, 10], CS methods are used by vectorizing the 3-D echo signal or rearranging each range slice 2-D signal into vector form, which are time-consuming and suffer from high memory cost. In [11], 2-D focused SAR images are obtained from each APC, and then CS or Bayesian CS method is implemented in the cross-track dimension. Due to the range course approximation, the above methods cannot get precise imaging results for large imaging scenes. In [9], a method combining 3-D pseudo-PFA with $L1$-norm minimization is introduced, which has the advantage of high reconstruction precision, low memory cost, etc..

However, the above CS-based methods assume scatterers to be located exactly on the pre-discretized grids. A practical 3-D SAR imaging scene, especially localized or distributed extended scene [14], is always a continuous field with scatterers scarcely on the exact grids, which will introduce the off-grid effect or model mismatch problem [15]. To solve the above problem, methods based on dictionary learning [16] or joint sparse recovery algorithms [14, 17] are proposed, but they are still established on the foundation of discrete dictionary or consider the high order Taylor approximation of the off-grid error. Besides, a modified $L1$-norm minimization algorithm is proposed to solve the model mismatch problem in wideband underwater sonar imaging [18], however, it is not suitable for the narrowband signal model in SAR imaging. By contrast, the model of atomic norm [19,20], which deals with sparse recovery problem directly on the continuous bearing space instead of discrete grids, has been studied in line spectral estimation and direction of arrival (DOA) estimation to solve the off-grid problem [19–21]. By reformulating the atomic norm minimization (ANM) as a semidefinite programming (SDP) problem, it provides not only a way to denoise the signal, but also an efficient signal recovery method. However, ANM has seldom been applied to SAR imaging due to the property of SAR echo signal, and to our knowledge hardly any literature analyzes the off-grid problem in CS-based methods for DLSLA 3-D SAR imaging.

In this paper, for DLSLA 3-D SAR with sparse and non-uniform APC distribution, we combine the 3-D pseudo-PFA with ANM, which not only possesses the merits of 3-D pseudo-PFA, i.e., high reconstruction precision (with the aid of wave front curvature phase error compensation), low computational and memory cost [7], but also eliminates the off-grid effect that exists in traditional CS-based methods for cross-track dimensional reconstruction. The proposed method considers the case with compressed measurements and takes the system noise into account, which is an innovative exploration. Besides, we analyze the off-grid effect and basis mismatch problem for DLSLA 3-D SAR, which will give a reference for system design and array configuration.

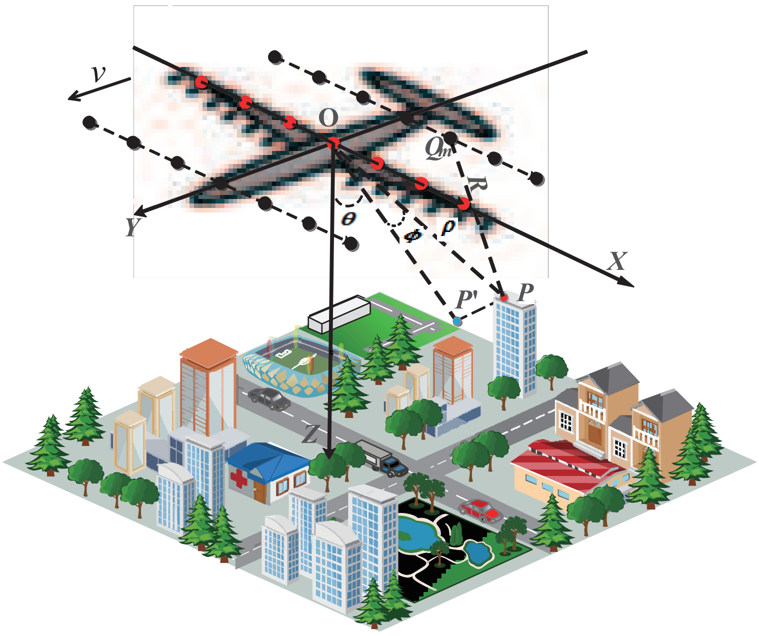

Figure 1 Imaging geometry of airborne DLSLA 3-D SAR.

2 Imaging principle for DLSLA 3-D SAR

2.1 Imaging geometry

The imaging geometry of airborne DLSLA 3-D SAR is shown in Figure 1. It operates nadir observation and uses a sparse linear array distributed along the wing of the platform, i.e., X axis, the cross-track dimension. By applying the MIMO array configuration, the linear array can achieve co-located transmit-receive APCs according to the equivalent phase center principle [8]. The theoretic APCs distribution should be uniform, which is usually not satisfied for practical system. The platform moves at altitude H with constant velocity v, with Y axis as its along-track dimension. The Z axis, which is perpendicularly downward to the XOY plane, represents the height dimension. The instantaneous position of the m-th APC is denoted by the vector $\boldsymbol{Q}_m = (x_m, y_n, 0), m \in [1, M], N \in [1, N_a]$, where x_m is the cross-track dimensional position of the APC, and y_n is the n-th sample in along-track dimension, with $y_n = v \times n \times \triangle t_y$ and $\triangle t_y$ representing the pulse repetition interval. For a target P in the 3-D imaging scene, whose coordinates are defined by the vector $\boldsymbol{r}_p = (x_p, y_p, z_p)$, P' is its projection onto XOZ plane and $\rho = \|\boldsymbol{r}_p\|_2$ is its distance from the coordinate origin, where $\|\cdot\|_2$ denotes the l_2-norm. With $\phi = \angle POP'$ and $\theta = \angle P'OZ$, the coordinates of P are $(x_p, y_p, z_p) = (\rho\cos\phi\sin\theta, \rho\sin\phi, \rho\cos\phi\cos\theta)$. At the n-th along-track sample instant, the distance between P and the m-th APC is $R(m, n; P) = \|\boldsymbol{Q}_m - \boldsymbol{r}_p\|_2$.

2.2 DLSLA 3-D SAR echo signal model

Suppose that the radar transmits a linear frequency modulated (LFM) signal with carrier frequency f_c, chirp rate K_r, pulse width T, then the echo signal after compensating for the phase error induced by the difference between the APCs and the real transceivers [11] can be expressed as

$$s_r(x_m, y_n, t) = \iiint_{P\in\Omega} \sigma(P) \times \mathrm{rect}\left(\frac{t - t_d}{T}\right) \times \exp\left\{-\mathrm{j}2\pi f_c t_d + \mathrm{j}\pi K_r (t - t_d)^2\right\} \mathrm{d}x_p\, \mathrm{d}y_p\, \mathrm{d}z_p, \quad (1)$$

where Ω is the support of the 3-D observed scene, $\sigma(P)$ represents the radar reflectivity of target P, $t_d = 2 \times R(m, n; P)/c$ is the time delay and c is the speed of light. After matched filtering, the range frequency domain signal can be written as

$$s_r(x_m, y_n, f_k) = \iiint_{P\in\Omega} \sigma(P) \times \exp\left\{-\mathrm{j}\frac{4\pi(f_c + f_k)}{c} R(m, n; P)\right\} \mathrm{d}x_p\, \mathrm{d}y_p\, \mathrm{d}z_p, \quad (2)$$

where $f_k \in [-K_rT/2, K_rT/2]$, $k \in [1, N_r]$, and N_r is the wave propagation dimension samples number.

Recall that

$$\begin{aligned} R(x_m, y_n; P) &= \sqrt{(x_m - \rho\cos\phi\sin\theta)^2 + (y_n - \rho\sin\phi)^2 + (0 - \rho\cos\phi\cos\theta)^2} \\ &= \rho - \frac{\boldsymbol{r}_p \cdot \boldsymbol{Q}_m}{\rho} + \sum_{i_1}\sum_{i_2} O(x_m^{i_1} \times y_n^{i_2}), \end{aligned} \tag{3}$$

where $\boldsymbol{r}_p \cdot \boldsymbol{Q}_m/\rho = x_m\cos\phi\sin\theta + y_n\sin\phi$, $\sum_{i_1}\sum_{i_2} O(x_m^{i_1} \times y_n^{i_2})$ with $i_1 + i_2 \geqslant 2$ are the high order expansion term, i_1 and i_2 are both non-negative integers. Defining $\rho' = \rho - x_m\cos\phi\sin\theta - y_n\sin\phi$ and inserting (3) into (2), we get

$$s_r(x_m, y_n, f_k) = \iiint_{P\in\Omega} \sigma(P_{\rho,\theta,\phi}) \times \exp\left\{-\mathrm{j}\frac{4\pi(f_c + f_k)}{c}\left(\rho' + \sum_{i_1}\sum_{i_2} O(x_m^{i_1} \times y_n^{i_2})\right)\right\} \mathrm{d}\rho\,\mathrm{d}\phi\,\mathrm{d}\theta. \tag{4}$$

2.3 3-D Pseudo-PFA

Define

$$\begin{aligned} s_o(x_m, y_n, f_k) &= \iiint_{P\in\Omega} \sigma(P_{\rho,\theta,\phi}) \times \exp\left\{-\mathrm{j}\frac{4\pi(f_c + f_k)}{c}\rho'\right\} \mathrm{d}\rho\,\mathrm{d}\phi\,\mathrm{d}\theta, \\ s_e(x_m, y_n, f_k) &= \exp\left\{-\mathrm{j}\frac{4\pi(f_c + f_k)}{c}\sum_{i_1}\sum_{i_2} O(x_m^{i_1} \times y_n^{i_2})\right\}, \end{aligned} \tag{5}$$

then $s_r(x_m, y_n, f_k) = s_o(x_m, y_n, f_k) \times s_e(x_m, y_n, f_k)$, where the last term represents the wave-front curvature phase error which will cause imaging distortion and defocus. By adopting the pseudo-polar formatting and compensating the wave-front curvature phase error, the radar reflectivity of the 3-D observed scene can be obtained by the endomorphism mapping principle of the pseudo-PFA [7],

$$\hat{\sigma}(\alpha, \beta, \gamma) = \sum_{m=1}^{M}\sum_{n=1}^{N_a}\sum_{k=1}^{N_r} \boldsymbol{P}[s_r(x_m, y_n, f_k)] \cdot \boldsymbol{P}[s_e^{\mathrm{H}}(x_m, y_n, f_k)] \cdot \exp\{\mathrm{j}2\pi(\alpha\hat{f}_k - \beta x'_m - \gamma y'_n)\}, \tag{6}$$

where the superscript H is the complex conjugate, $\boldsymbol{P}[\cdot]$ represents the pseudo-polar formatting, $x'_m = x_m(f_c + f_k)/f_c$, $y'_n = y_n(f_c + f_k)/f_c$, $\hat{f}_k = f_c + f_k$, and α, β, γ have the following expression respectively,

$$\alpha = \frac{2\rho}{c}, \quad \beta = \frac{2\cos\phi\sin\theta}{\lambda_c}, \quad \gamma = \frac{2\sin\phi}{\lambda_c}, \tag{7}$$

where $\lambda_c = c/f_c$ is the nominal radar wavelength. Obviously, the 3-D pseudo-polar coordinate image in (α, β, γ) domain can be obtained by the kernel of a 3-D Fourier transform with respect to $(\hat{f}_k, x'_m, y'_n)$. The corresponding Cartesian coordinates of (x, y, z) can be obtained by interpolating as

$$x = \frac{\lambda_c c}{4}\alpha\beta\,, \quad y = \frac{\lambda_c c}{4}\alpha\gamma\,, \quad z = \frac{\lambda_c c}{4}\sqrt{\frac{4}{\lambda_c^2} - \beta^2 - \gamma^2}. \tag{8}$$

However, the practical DLSLA 3-D SAR system is often subject to possible channel failure or array design imperfection, which leads to a sparse and non-uniform virtual APCs distribution. Then the cross-track FFT of the 3-D FFT kernel for (6) cannot be used.

3 3-D imaging scene reconstruction by sparse recovery method

After applying a wave propagation and along-track 2-D FFT to the pseudo-polar formatted signal, the α and β dimensional focused 3-D signal turns into

$$\begin{aligned} U(\alpha, x'_m, \gamma) &= \int \sigma(\alpha, \beta, \gamma) \cdot \mathrm{sinc}(B_r\alpha) \cdot \mathrm{sinc}(L_a\gamma) \cdot \exp\{\mathrm{j}2\pi\beta x'_m\}\,\mathrm{d}\beta \\ &= \int \hat{\sigma}(\alpha, \beta, \gamma)\exp\{\mathrm{j}2\pi\beta x'_m\}\,\mathrm{d}\beta, \end{aligned} \tag{9}$$

where B_r is the signal bandwidth, L_a is the cross-track virtual array length, and $\hat{\sigma}(\alpha, \beta, \gamma)$ is the radar reflectivity coefficient needed to be recovered.

3.1 Sparse property analysis for different kinds of targets

We know that an imaging scene usually contains different kinds of targets, including point targets, localized or distributed extended targets [14], and volumetric scatterers [3]. Point targets mainly include dihedral or trihedral reflectors, metallic structures, etc., and extended targets often refer to urban buildings or mountainous areas. For DLSLA 3-D SAR imaging geometry, these two kinds of targets behave typically pixel-wise spatial sparsity, i.e., each along-track and wave propagation pixel contains only a limited number of dominating scatterers compared with the total cross-track dimension. Nevertheless, for volumetric targets or rough surface, e.g., vegetated areas, the pixel-wise sparsity in the spatial domain is rarely true. However, a proper sparse basis, e.g., wavelet basis, can be utilized to represent the scene sparsely in the corresponding domain [3]. Thus, unlike traditional 2-D SAR, the 3-D SAR imaging scene usually has a sparse representation in a certain domain. In this paper, we mainly consider the scenes of point targets and extended targets, whereas volumetric scatterers are left for further study.

3.2 On-grid CS

In the framework of traditional CS, to recover the sparse signal we usually discretize the potential space in equal grids and assume the true scatterers located exactly on the pre-discretized grids. Recall (9) and suppose that the true locations of scatterers in β dimension are $\boldsymbol{\beta}_{\mathrm{true}} = [\beta_1, \beta_2, \ldots, \beta_K]$, where K is the number of the scatterers. For convenience, we use U_m and $\hat{\sigma}(\beta)$ to represent $U(\alpha, x'_m, \gamma)$ and $\hat{\sigma}(\alpha, \beta, \gamma)$, respectively. After dividing β domain into equal grids as $\boldsymbol{\beta} = [\beta'_1, \beta'_2, \ldots, \beta'_L]$ with $L \gg K$, for each (α, γ) pixel, Eq. (9) can be expressed as

$$U_m = \sum_{i=1}^{L} \hat{\sigma}(\beta'_i) \exp(\mathrm{j}2\pi\beta'_i x'_m), \tag{10}$$

and the matrix expression for each (α, γ) pixel is

$$\boldsymbol{U}_m = \boldsymbol{R} \cdot \boldsymbol{e} + \boldsymbol{\varepsilon}, \tag{11}$$

where $\boldsymbol{U}_m = [U_1, U_2, \ldots, U_{N_e}]^{\mathrm{T}}$, N_e is the number of APCs, $\boldsymbol{e} = [(\hat{\sigma}(\beta'_1), \hat{\sigma}(\beta'_2), \ldots, \hat{\sigma}(\beta'_L)]^{\mathrm{T}}$ is the zero-padded version of signal $\hat{\sigma}(\beta)$ from $\boldsymbol{\beta}_{\mathrm{true}}$ to $\boldsymbol{\beta}$, $\boldsymbol{\varepsilon}$ is the noise and $\boldsymbol{R}$ is the measurement matrix with the m-th row and i-th column element $r_{mi} = \exp(\mathrm{j}2\pi\beta'_i x'_m)$. When there is no priori knowledge of K and in the presence of noise, the under-determined equation can be solved by convex L1-norm minimization [2],

$$\hat{\boldsymbol{e}} = \arg\min_{\boldsymbol{e}} (\|\boldsymbol{U}_m - \boldsymbol{R} \cdot \boldsymbol{e}\|_2^2 + \delta \|\boldsymbol{e}\|_1^2), \tag{12}$$

where δ is the regularization parameter. If $\boldsymbol{\beta}_{\mathrm{true}} \subset \boldsymbol{\beta}$ holds, the on-grid CS can give exact reconstruction, i.e., if $\beta_n = \beta'_i$ then $\hat{\sigma}(\beta'_i) = \hat{\sigma}(\beta_n)$, otherwise, $\hat{\sigma}(\beta'_j) = 0$. However, when scatterers are not coincident with the pre-discretized grids, i.e., $\boldsymbol{\beta}_{\mathrm{true}} \not\subseteq \boldsymbol{\beta}$, then the off-grid effect will arise. Analysis in [15] shows that any off-grid scatterer located between two adjacent grids will spill non-zero values into all grids with the amplitude following a Dirichlet kernel, which will highly deteriorate the reconstruction performance.

3.3 Measurement matrix coherence property and basis mismatch analysis

To remedy the off-grid effect we may attempt to use a denser grid, however, it will in turn greatly increase the coherence of the measurement matrix for reliable sparse recovery [13]. Known from Eq. (10), $\boldsymbol{R}$ approximates a random partial Fourier matrix when the APCs are equally spaced. In most cases, the APCs follow a randomly uniform distribution and the coherence [13] of $\boldsymbol{R}$ is defined as

$$\mu(\boldsymbol{R}) = \mu(r_k, r_p) = \max_{1 \leqslant k, p \leqslant L, k \neq p} \frac{|\langle r_k, r_p \rangle|}{\|r_k\|_2 \|r_p\|_2}. \tag{13}$$

Inserting the expression of r_k and r_p, i.e., the k-th and p-th columns of matrix $\boldsymbol{R}$, into (13), yields

$$\mu(\boldsymbol{R}) = \max_{1 \leqslant k, p \leqslant L, k \neq p} \left| \sum_{m=1}^{N_e} \exp\{\mathrm{j}2\pi x'_m (\beta'_k - \beta'_p)\} \right| \Big/ N_e. \tag{14}$$

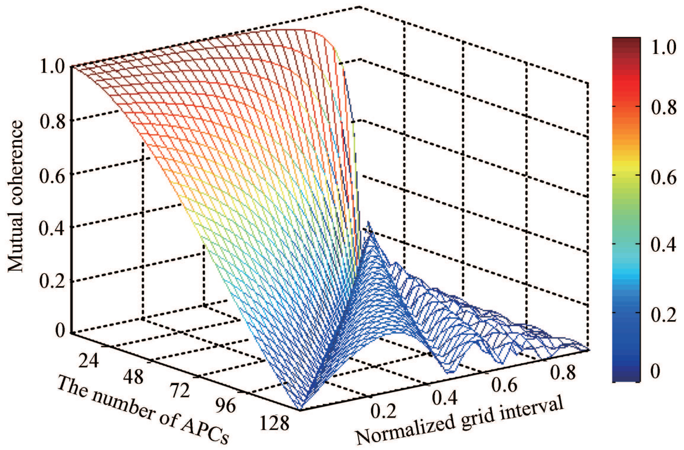

Figure 2 Mutual coherence versus grid interval and sample number.

We know that the lower the level of mutual coherence, the better the reconstruction performance. Figure 2 illustrates the mutual coherence versus grid interval and sample number in the case of uniformly distributed APCs. From Figure 2 and Eq. (14) we know that for DLSLA 3-D SAR, large scene grids and sufficient APCs will guarantee the low coherence. Besides, the above analysis is based on the assumption that the transmitting waveform is LFM signal which has a relatively poor incoherence performance compared with those waveforms obeying a specific Gaussian distribution, such as random signal or OFDM signal [22]. Thus, considering the incoherence property, computational complexity and imaging performance, a finer gridding is still not an advisable remedy for the off-grid effect. Besides, just like that in the frequency mismatch, damping factors [15] may also exist in the measurement matrix $\boldsymbol{R}$ and this kind of mismatch cannot be remedied by choosing proper girds in the framework of traditional CS.

3.4 Atomic norm and continuous CS

Unlike the traditional CS, ANM has been proposed to work in the continuous domain to eliminate the off-grid effect, and this kind of sparse reconstruction approach is referred to as continuous CS [19–21]. Suppose we observe a signal which is a superposition of a few complex sinusoids,

$$x_m^o = \sum_{k=1}^{K} c_k \mathrm{e}^{\mathrm{j}2\pi f_k m}, \quad m \in [M], \tag{15}$$

where the support of K normalized frequencies is $\boldsymbol{f} = [f_1, f_2, \ldots, f_K] \subset [0,1]$, $c_k \in \mathbb{C}$ is the complex amplitude, $[M] \triangleq [0, \ldots, M-1]$ or $[-\lfloor \frac{M}{2} \rfloor, \ldots, \lfloor \frac{M}{2} \rfloor - 1]$ is an index with the length M, and $\lfloor \cdot \rfloor$ means rounding towards the nearest integer. Instead of observing x_m^o on the whole index $[M]$, we have only a portion set $\boldsymbol{\Omega} \subset [M]$ with $L \triangleq |\boldsymbol{\Omega}| \leqslant M$. Continuous CS is to recover complete support set $\boldsymbol{x} = [x_m^o] \in \mathbb{C}^M$ in the continuous domain with the measurements on the subset $\boldsymbol{x}^o$. Define atoms $\boldsymbol{a}(f,\varphi) \in \mathbb{C}^M, f \in [0,1], \varphi \in [0, 2\pi)$ as

$$[\boldsymbol{a}(f,\varphi)]_m = \mathrm{e}^{\mathrm{j}2\pi f m + \mathrm{j}\varphi}, \ m \in M. \tag{16}$$

Then Eq. (15) can be rewritten as

$$\boldsymbol{x}^o = \sum_{k=1}^{K} |c_k| \, \boldsymbol{a}(f_k, \varphi_k), \tag{17}$$

where $\varphi_k \in [0, 2\pi)$ is the phase of the k-th scatterer whose amplitude is $|c_k|$. The atomic set $\mathcal{A} = \{\boldsymbol{a}(f,\varphi) : f \in [0,1], \varphi \in [0, 2\pi)\}$ is defined as the simplest building blocks of the raw signal, the same way as one-sparse vectors for sparse signals and unit-norm rank-one matrices for low-rank matrices [19]. Then atomic norm is defined as the gauge function of the hull of $\mathcal{A}$:

$$\begin{aligned}\| \boldsymbol{x} \|_{\mathcal{A}} &= \inf\{t > 0 : \boldsymbol{x} \in t \cdot \mathrm{conv}(\mathcal{A})\} \\ &= \inf_{\substack{|c_k| \geqslant 0 \\ \varphi_k \in [0,2\pi) \\ f_k \in [0,1]}} \left\{ \sum_k |c_k| : \boldsymbol{x} = \sum_k |c_k| \, \boldsymbol{a}(f_k, \varphi_k) \right\}. \end{aligned} \tag{18}$$

Due to the fact that low-dimensional faces of $\mathrm{conv}(\mathcal{A})$ correspond to signals involving only a few atoms, the atomic norm can derive sparsity of the signal [19]. In the framework of continuous CS, only a subset of entries $\boldsymbol{\Omega} \subset [\boldsymbol{M}]$ is observed and the missing samples subset $\boldsymbol{\Omega}^C = [M] \backslash \boldsymbol{\Omega}$ can be estimated by ANM,

$$\min_{\boldsymbol{x}} \ \|\boldsymbol{x}\|_{\mathcal{A}} \quad \text{s.t.} \ \ x_m = x_m^o \ , \ \ m \in \boldsymbol{\Omega}. \tag{19}$$

Eq. (19) can be equivalently solved by an exact SDP, then dual polynomial can be used for identifying the frequencies. For more details, readers can refer to [19].

3.5 Robust off-grid scatterers reconstruction by atomic norm minimization

Without loss of generality, next we consider the case with both compressed and contaminated measurements, which is not much studied in the common application of ANM. By combining the compression with noise, Eq. (17) turns into the matrix expression form,

$$\boldsymbol{y} = \varPhi \boldsymbol{x} + \boldsymbol{w}, \tag{20}$$

where $\varPhi \in \mathbb{R}^{L\times M}$ is the sparse representing matrix that is an identical matrix for the sparse signal, and $\boldsymbol{w} \in \mathbb{C}^L$ is the noise. Then, the atomic norm optimization can be used to reconstruct $\boldsymbol{x}$ from $\boldsymbol{y}$,

$$\min_{\boldsymbol{x}} \frac{1}{2} \|\boldsymbol{y} - \varPhi \boldsymbol{x}\|_2^2 + \tau \|\boldsymbol{x}\|_{\mathcal{A}}, \tag{21}$$

where τ is the regularization parameter. In the framework of bounded real lemma, the above atomic norm optimization problem can be solved by the following equivalent SDP [20, 21]:

$$\min_{q,\boldsymbol{x},\boldsymbol{u}} \frac{1}{2} \|\boldsymbol{y} - \varPhi \boldsymbol{x}\|_2^2 + \frac{1}{2}\tau \{\mathrm{tr}(\boldsymbol{T}(\boldsymbol{u})) + q\} \quad \text{s.t.} \quad \begin{bmatrix} \boldsymbol{T}(\boldsymbol{u}) & \boldsymbol{x} \\ \boldsymbol{x}^{\mathrm{H}} & q \end{bmatrix} \succeq 0, \tag{22}$$

where $\boldsymbol{T}(\boldsymbol{u}) \in \mathbb{C}^{L\times L}$ is the Hermitian Toeplitz matrix with its input $\boldsymbol{u} \in \mathbb{C}^L$, $\mathrm{tr}(\cdot)$ denotes the trace. The SDP problem can be solved efficiently by many mature Matlab solvers such as CVX [23]. Then dual optimization is implemented to identify the frequencies in the recovered signal [21]. The dual norm $\|\cdot\|_{\mathcal{A}}^*$ of the atomic norm that lies in a finite dimensional set is defined as

$$\|\boldsymbol{z}\|_{\mathcal{A}}^* = \sup_{\boldsymbol{a}\in\mathcal{A}} \langle \boldsymbol{z}, \boldsymbol{a} \rangle_{\mathrm{Re}} \,, \tag{23}$$

where $\langle \boldsymbol{z}, \boldsymbol{a} \rangle_{\mathrm{Re}} = \mathrm{Re}(\boldsymbol{z}^{\mathrm{H}} \boldsymbol{a})$ represents the real inner product. Suppose $\hat{\boldsymbol{z}} = \varPhi^{\mathrm{H}}(\boldsymbol{y} - \varPhi \hat{\boldsymbol{x}})$ where $\hat{\boldsymbol{x}}$ is the optimal solution of (22), then $\hat{\boldsymbol{z}}$ is the solution to the dual problem of (21) on the foundation of the strong duality. According to the dual problem lemma proofed by [20], the solution for the frequency support set of (20), defined by S, satisfies that

$$\begin{cases} |\langle \hat{\boldsymbol{z}}, \boldsymbol{a} \rangle| < \tau, & \forall \boldsymbol{a} \notin S, \\ \langle \hat{\boldsymbol{z}}, \boldsymbol{a} \rangle = \tau, & \forall \boldsymbol{a} \in S, \end{cases} \tag{24}$$

i.e., the frequency support could be identified by finding the maximums of the inner product of $\hat{\boldsymbol{z}}$ and all the atoms. After identifying the frequencies, the debiased amplitudes can be obtained by the least square method. Since the atoms lie in the continuous domain, the estimated frequency support is guaranteed to be a compact set [19], therefore, the off-grid effect in traditional CS will no longer exist.

3.6 Combine 3-D pseudo-PFA with atomic norm minimization for DLSLA 3-D SAR imaging

To apply the ANM to DLSLA 3-D SAR cross-track imaging, we firstly formulate (9) with a proper set of atoms. Suppose that the number of scatterers in a (α,γ) pixel is K, then Eq. (9) can be expressed as

$$U_m = \sum_{i=1}^{K} \hat{\sigma}(\beta_i)\exp(\mathrm{j}2\pi\beta_i x'_m)\,,\ \ m\in[N_e]\,, \tag{25}$$

where $[N_e]$ is the measurements index with length N_e. Insert $x'_m = m\cdot d'$ into (25) with d' as the resampled interval of the cross-track APCs. Multiplying both sides of (25) with exponential term $\exp(\mathrm{j}\pi m)$ and considering the noise, we have

$$S_m = \sum_{i=1}^{K} \hat{\sigma}(\beta_i)\exp(\mathrm{j}2\pi f_i m) + w_m, \tag{26}$$

where $S_m = U_m\cdot\exp(\mathrm{j}\pi m)$, $f_i = \beta_i\cdot d' + \frac{1}{2}$ and w_m is the additive noise.

According to the DLSLA 3-D SAR system parameters and the unambiguous imaging conditions referred in [7], we know that the normalized frequency satisfies $f_i\in[0,1]$. Owing to the spatial sparse feature of the 3-D imaging scene, the sparse representing matrix Φ is a binary sample matrix. Thus, the expression (26) falls into the model of ANM. Then we can get f_i and further β_i by solving the SDP problem in (22) and finding the maximums of the dual polynomial by (24). After that, the scatterer's coefficient $\hat{\sigma}(\beta_i)$ can be easily obtained by the least square method.

3.7 Robust reconstruction conditions analysis

(1) Regularization parameter estimation

As shown in (22), to exactly resolve the SDP problem, the regularization parameter τ should be a prior information, which depends on the dual atomic norm of the noise [21]. Supposing that the additive noise follows the Gaussian distribution $\mathcal{N}(0,\ \sigma_n^2)$, if the optimal regularization parameter is chosen as the upper bound of the dual atomic norm, then it follows

$$\tau = \sigma_n\left(1+\frac{1}{\lg(M)}\right)\sqrt{M\lg(M)+M\lg(4\pi\lg(M))}. \tag{27}$$

In a practical SAR system, the noise variance σ_n^2 is not a priori and needs to be estimated from the measurements. Combining the property of line spectral estimation with SAR imaging, the estimation of σ^2 can be obtained by methods proposed in [11, 16, 21].

(2) Resolution and sampling number analysis

Recall that the APC index set is

$$[N_e]\subset[M] = \left\{-\left\lfloor\frac{M}{2}\right\rfloor,\ldots,\left\lfloor\frac{M}{2}\right\rfloor-1\right\}$$

with origin at the middle point of the linear array, and the elements of set $[N_e]$ can be obtained by selecting from $[M]$. According to the analyses and results in [19, 20], when the APC samples follow a uniform distribution or Bernoulli distribution, the minimum separable location in β dimension satisfies

$$\Delta\beta = \min_{k\neq j}|\beta_k-\beta_j| \geqslant \frac{c_1}{\lfloor (M-1)/4\rfloor\cdot d'} \tag{28}$$

for some small universal constant c_1, then there exists a numerical constant C so that

$$N_e \geqslant C\max\left\{\lg^2\frac{M}{\eta}, K\lg\frac{K}{\eta}\lg\frac{M}{\eta}\right\} \tag{29}$$

Table 1 Simulation parameters

Parameters	Value	Parameters	Value
Carrier frequency	37.5 GHz	Signal bandwidth	250 MHz
Platform fly height	1500 m	Range sampling number	2500
AT[a)] sampling number	236	AT sampling interval	0.015 m
Filled array CT[b)] APC number	236	CT sampling interval	0.015 m
AT beam width	14°	CT beam width	14°

a) AT is short for along-track; b) CT is short for cross-track

is enough to reconstruct the scatterers in β dimension by solving the SDP problem (22) with probability at least $1-\eta$ [19,20]. In the case of non-uniform samples, the achievable resolution may break the above restriction [21], i.e., when the APCs distribute sparsely and non-uniformly, the ANM may achieve a much higher resolution than the restriction in (28). Moreover, if we want to achieve comparable resolution, it also provides a reduction in the number of APCs when designing the array configuration.

4 Experiments and results

In this section, three experiments are presented to illustrate the performance of our proposed method. Point targets and distributed scene are provided to evaluate the effectiveness. All experiments are performed in MATLAB v8.3.0 environment, and CVX [23] is used to solve the SDP.

4.1 Cross-track multiple scatterers reconstruction performance analysis

(1) Reconstruction performance comparisons

For a practical imaging scene, usually more than one scatterer is located in the same wave propagation and along-track resolution cell, i.e., after pseudo-polar formatting they are inside the same (α,γ) pixel. In the first experiment we assume that there are three scatterers inside one (α,γ) pixel and compare the reconstruction performance of different methods. The three scatterers' amplitudes are all equal to 1 and their phases follow uniform distribution. The first two scatterers are located within one β dimensional Rayleigh resolution and the third one is more than one resolution cell apart from them. The simulation parameters are listed in Table 1. We randomly choose 50% APCs from the filled virtual array and consider the signal to noise ratio (SNR) 30 dB. After pseudo polar fomatting, we implement the ANM, L1-norm minimization and multiple signal classification (MUSIC) for β dimensional reconstruction. For L1-norm minimization, we use the iterative thresholding algorithms (IST) [24] for implementation and the grid interval is set as $\Delta g = \mathrm{factror}\cdot\rho_{f_{\mathrm{nor}}}$, where $\rho_{f_{\mathrm{nor}}}$ is the normalized frequency Rayleigh resolution and the parameter factor is assigned to $\{1, 1/2, 1/4\}$ in the following simulations respectively. The normalized frequencies f_{nor}, which are transformed from β dimensional locations by (26), are guaranteed to have a shift from the pre-discretized grids. Figure 3 shows the reconstruction results of the normalized frequencies. ANM outperforms L1-norm minimization both in frequencies location and amplitude estimation, and it is shown that a finer grid is not an advisable remedy for the off-grid effect. Compared with MUSIC, ANM has no sidelobes and does not need the scatterer number as a priori. Thus, in the following experiments we only use ANM and L1-norm minimization with grid factor = 1 for comparison.

(2) Quantitative comparisons

Quantitative comparisons are carried out in the following experiments to evaluate the algorithms. We use four scatterers located at $(-8.2\ \mathrm{m}, 100\ \mathrm{m}, 1500\ \mathrm{m})$, $(-6.5\ \mathrm{m}, 100\ \mathrm{m}, 1500\ \mathrm{m})$, $(16.4\ \mathrm{m}, 100\ \mathrm{m}, 1500\ \mathrm{m})$, $(45.2\ \mathrm{m}, 100\ \mathrm{m}, 1500\ \mathrm{m})$ for simulation. The reflectivity coefficient of the fourth scatterer is only 1/3 of the other three scatterers. Figure 4 shows the results under three different SNRs, and for display convenience, we only give the cross-track profile of the reconstructed targets. We see that when SNR is as low as 5 dB, the proposed method cannot give accurate reconstruction. When SNR increases to 25 dB, the proposed method can reconstruct not only the closely separated scatterers but also the weak target, while the method combining pseudo-PFA with L1-norm minimization (pseudo-PFA-L1) still suffers from off-grid effect. Furthermore, to quantize the performance under different SNRs and sampling

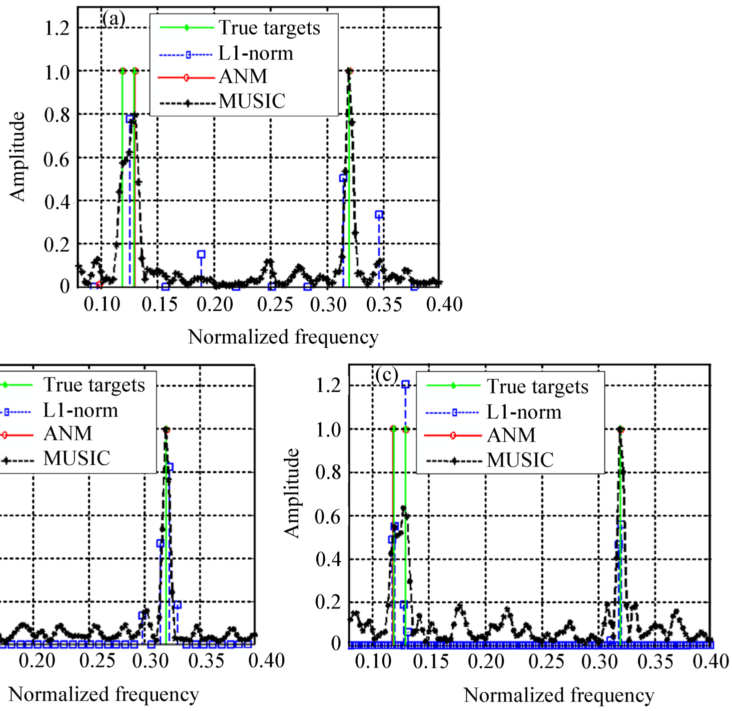

Figure 3 Normalized frequencies reconstruction results by ANM, L1-norm minimization and MUSIC, respectively. For L1-norm minimization, the grid interval factor is (a) 1; (b) 1/2; (c) 1/4.

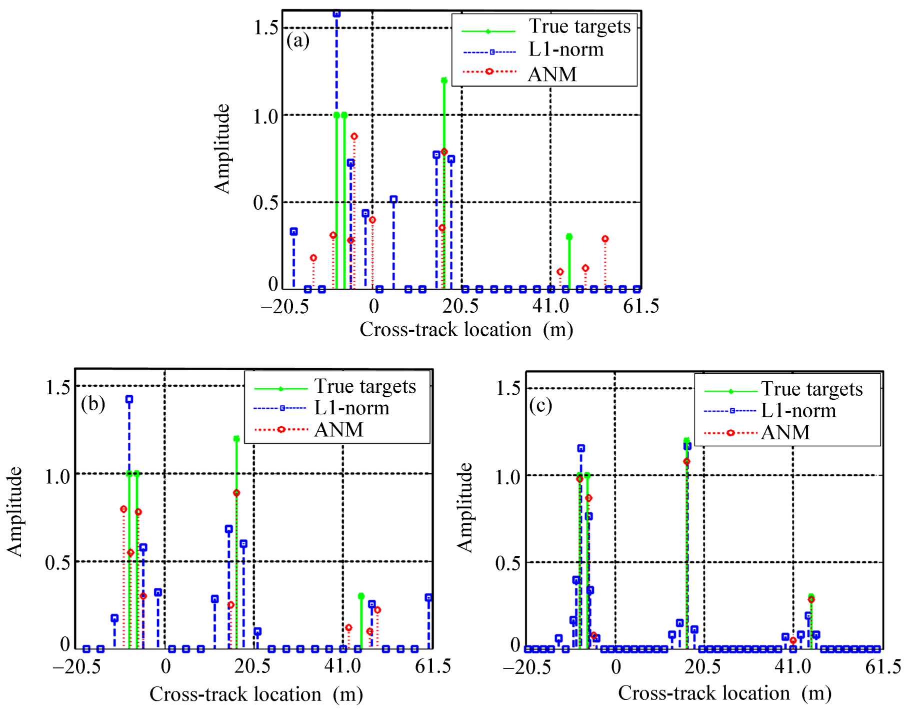

Figure 4 Cross-track profile of reconstruction results with different SNRs: (a) 5 dB; (b) 15 dB; (c) 25 dB.

numbers, we give the statistical performance via 100 Monte Carlo trials by the mean square error (MSE) of the cross-track location estimation, which is defined as the error between the reconstructed locations and the true locations. Since the cross-track dimensional target reconstruction of the proposed method is a problem of parameters estimation, Cramer-Rao lower bound (CRLB) is a common benchmark to

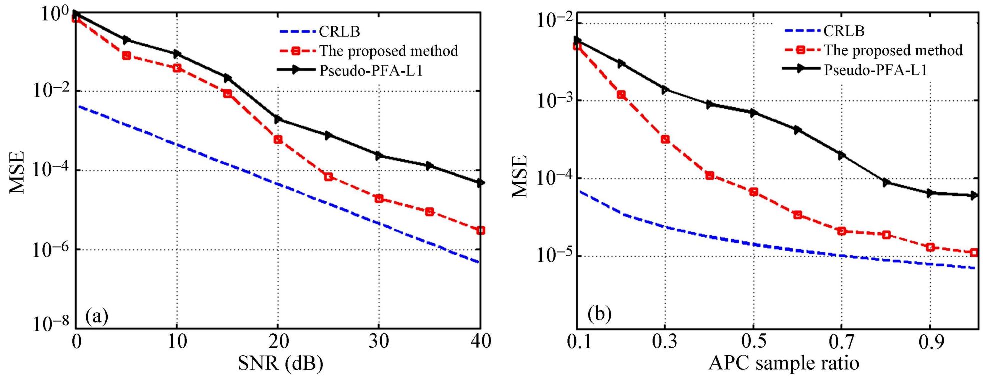

Figure 5 (Color online) (a) MSE vs SNR; (b) MSE vs APC sample ratio.

evaluate the performance. Supposing that the noise is Gaussian white noise and the APCs follow uniform distribution, the CRLB of cross-track single target location is asymptotical [2, 25]:

$$\mathrm{CRLB}(\hat{x_p}) = \frac{3}{2\pi^2}\frac{(\rho_{\hat{x_p}})^2}{N_e \cdot \mathrm{SNR}}, \tag{30}$$

where $\rho_{\hat{x_p}}$ is the cross-track resolution in Cartesian coordinate, $\mathrm{SNR} = (\sigma(\hat{x_p})/\sigma_n)^2$ is the target signal to noise ratio. The CRLB of location estimation is a little different from (30) when there are multiple scatterers to estimate. While suppose that the scatterers are uncorrelated and the Fisher information matrix has no coupling, the difference is slight [2, 25]. We can use (30) as a rough benchmark to evaluate the performance of targets reconstruction in cross-track dimension.

Figure 5(a) gives the MSE in the presence of Gaussian white noise with different SNRs under APC sparsity ratio (defined as the value of N_e/M) 0.5. We see that when SNR is low, both the proposed method and pseudo-PFA-L1 have high errors. As the SNR increases to 25 dB, the MSE of the proposed method is obviously lower than pseudo-PFA-L1. When SNR becomes larger, both algorithms have lower errors, but the proposed method still has a better performance than pseudo-PFA-L1, which still suffers from off-grid effect. Figure 5(b) shows the MSE under different APC sparsity ratios and the SNR of Gaussian white noise is 25 dB. We can see that with fewer APCs the proposed method can achieve more satisfactory results than pseudo-PFA-L1, which is in accordance with the analysis in Section 3.

Next, we will compare the computational complexity of the algorithms. It is known that the pseudo-PFA is computationally effective, thus, the main computational time is determined by the cross-track reconstruction algorithm. In the experiment with SNR=25 dB and APC sample ratio 0.5, for the cross-track reconstruction of one (α, γ) pixel, it takes about 19 s to use ANM, while about 1.1 s to implement L1-norm minimization by IST. We know that when using CVX to solve the SDP in ANM, it uses SDPT3 solver and adopts the interior point methods to solve the program [23, 26]. For interior-point methods, the number of iterations is usually small and the most expensive step in each iteration is the computation of the Schur complement. The computational complexity of different path-following algorithms of interior-point methods are slightly different, but they are rough on the order of $\mathrm{O}(M^2 \cdot N^2 + N_e \cdot M^3)$. Results in [19] show that the computational burden of ANM approximates that of basis pursuit (BP), which is higher than that of IST, a fast reconstruction algorithm with computational complexity about $\mathrm{O}(M \cdot N_e + M \cdot \log M)$. Considering the reconstruction performance, it is acceptable to use ANM for 3-D scene reconstruction. Interested readers can refer to [19–21] for some fast methods to approximate ANM.

4.2 DLSLA 3-D SAR imaging of point targets

In this subsection, point targets simulation is shown to verify the proposed method for DLSLA 3-D SAR imaging. Simulated parameters are listed in Table 1. There are eight scatterers with the unit reflectivity in the Cartesian coordinate system, as shown in Figure 6(a). After transforming (X, Y, Z) coordinates into (α, β, γ) domain, the projection image onto $\beta\gamma$ plane is shown in Figure 7(a). For pseudo-PFA-L1 the

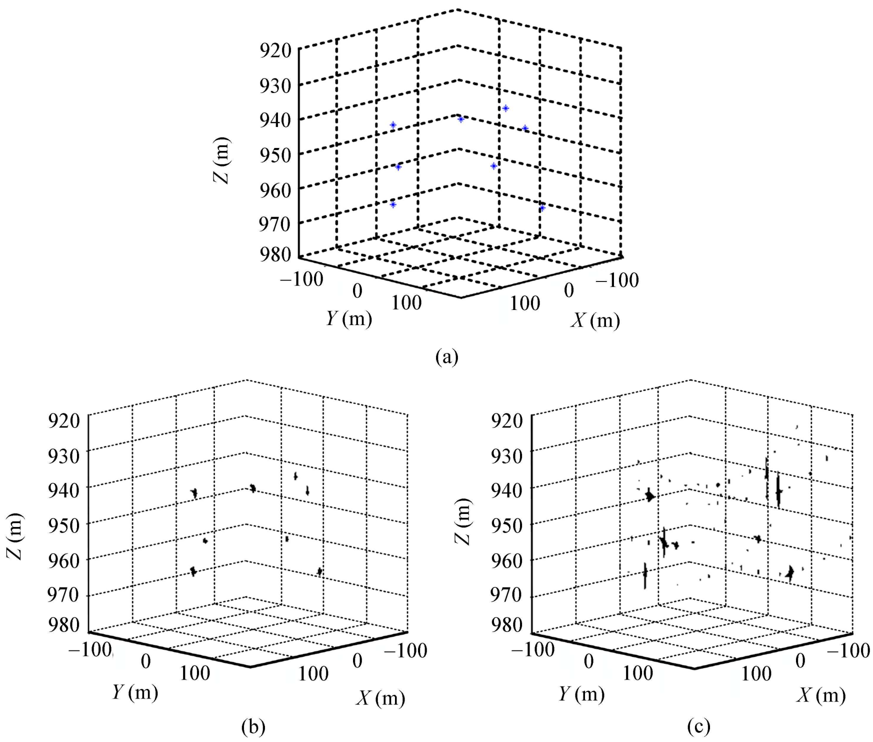

Figure 6 (a) Point targets locations in (X, Y, Z) coordinate system. 3-D imaging result (top 15 dB magnitude) by (b) the proposed method; (c) pseudo-PFA-L1.

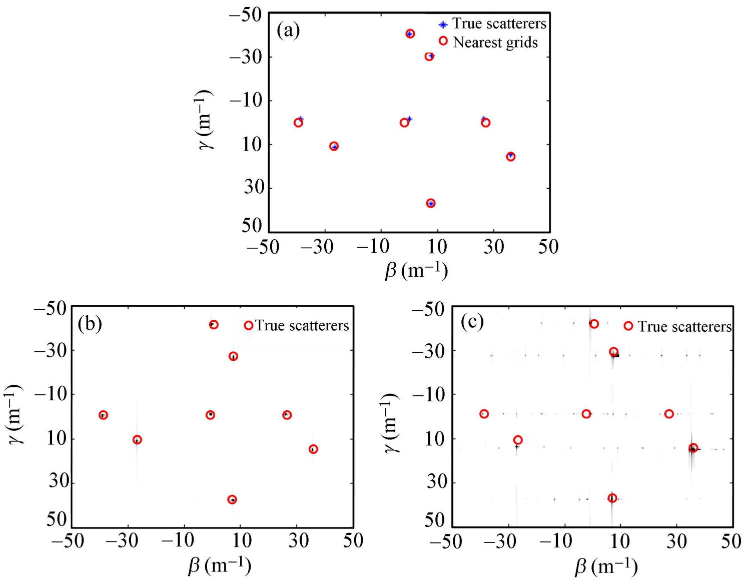

Figure 7 (a) Projection of the true scatterers onto $\beta\gamma$ plane compared with the nearest grids. Imaging projection (black spots) onto $\beta\gamma$ plane by (b) the proposed method; (c) pseudo-PFA-L1.

discretized grid interval is chosen as the Rayleigh resolution [7] $\delta_\beta = 0.89/L_e$, where L_e is the length of the cross-track array. Figure 7(a) shows that on $\beta\gamma$ plane there are scatterers off the grids. We randomly choose 50% APCs from the filled virtual array and the SNR is 25 dB.

The projection of the 3-D polar reconstructed images onto $\beta\gamma$ plane by the proposed method and pseudo-PFA-L1 are shown in Figure 7(b) and (c), respectively. The 3-D imaging result in (X, Y, Z) coordinate system by the proposed method is shown in Figure 6(b), and Figure 6(c) gives the corresponding

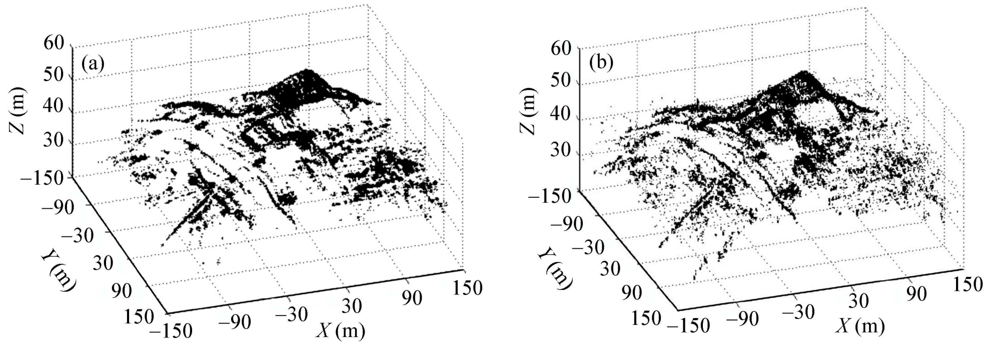

Figure 8 3-D reconstructed image in (X, Y, Z) coordinate system by (a) the proposed method; (b) pseudo-PFA-L1.

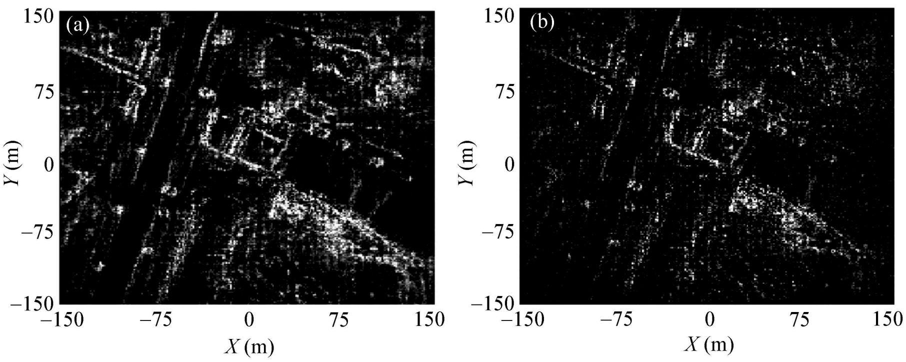

Figure 9 XY plane projection image by (a) the proposed method; (b) pseudo-PFA-L1.

result by pseudo-PFA-L1. Figures 6 and 7 indicate that when the off-grid effect and noise exist, the reconstructed result from the traditional CS suffers from lots of spurious and inaccurate scatterers. By contrast, the proposed method can perform a much more satisfactory reconstruction result. The total time for the 3-D scene reconstruction by the proposed method is about 81 h, while about 5.7 h by the pseudo-PFA-L1 that uses IST for L1-norm minimization.

4.3 DLSLA 3-D SAR imaging of distributed extended targets

In this subsection, an airborne CSAR 2-D image and its DEM data [4] are used to simulate the distributed scene. The scene has the extent of 300 m $\times$ 300 m $\times$ 40 m in the Cartesian coordinate system with the system parameters listed in Table 1. The along-track coordinate (Y dimension) of scatterers is uniformly distributed in [-150 m, 150 m] with interval 1.5 m. To simulate the off-grid scatterers, the cross-track coordinate (X dimension) of scatterers has a $\pm 10\%$ random deviation from the uniform distribution [-150 m, 150 m] with interval 1.5 m. The grid interval for pseudo-PFA-L1 is chosen as the β dimensional Rayleigh resolution, therefore, after transformed into (α, β, γ) domain, off-grid scatterers exist in the simulated scene. 50% APCs are randomly selected from the filled virtual array and the two APCs at both ends of the virtual array are always left out to guarantee the total array length. The SNR is chosen as 25 dB. The 3-D reconstructed image in (X, Y, Z) coordinate system by the proposed method is shown in Figure 8(a), and Figure 8(b) gives the corresponding result from pseudo-PFA-L1. The orthogonal projection images onto the XY plane by the two methods are illustrated in Figure 9. Obviously, pseudo-PFA-L1 method suffers from many spurious reconstructed scatterers and loses many image details for the distributed extended scene with off-grid scatterers. By contrast, the proposed method shows better image contrast and much clearer shape of road, hydropower station, etc.

5 Discussion and conclusion

DLSLA 3-D SAR whose imaging scene shows sparsity in a certain domain, can exploit the sparse recovery technique to achieve cross-track dimensional high resolution in the case of sparse and non-uniform cross-track APCs distribution. This paper analyzes the off-grid effect of traditional CS and proposes a method exploiting the 3-D pseudo-PFA and atomic norm minimization (ANM) for DLSLA 3-D SAR imaging. By transforming the atomic norm optimization as an SDP, the proposed method can avoid the off-grid effect and achieve continuous sparse signal reconstruction. The sparse reconstruction method provides a reference for practical array design, i.e., to achieve a comparable performance we may no longer need a filled cross-track virtual array, which will decrease the system burden and expense. Moreover, the paper gives the conditions that can guarantee the cross-track dimensional exact reconstruction. The method is suitable for DLSLA 3-D SAR imaging of point targets and extended scenes which both behave spatial sparsity. The experiments verify the imaging performance and the robustness of the proposed method. For volumetric scatterers scene that needs a proper spare representation basis such as wavelet basis, the atomic norm approach may also perform better than the traditional CS, which needs further study.

Acknowledgements The work was supported by Innovation of the Chinese Academy of Sciences International Partnership Project (Grant No. Y313110240), National Natural Science Foundation of China (Grant Nos. 61201433, 61372186), and Program for Young Talents of Science and Technology in Universities of Inner Mongolia Autonomous Region (Grant No. NJYT-14-B09).

Conflict of interest The authors declare that they have no conflict of interest.

References

1 Soumekh M. Synthetic Aperture Radar Signal Processing with Matlab Algorithms. New York: Wiley, 1999
2 Zhu X, Bamler R. Super-resolution power and robustness of compressive sensing for spectral estimation with application to spaceborne tomographic SAR. IEEE Trans Geosci Remote Sens, 2012, 50: 247–258
3 Aguilera E, Nannini M, Reigber A. Wavelet-based compressed sensing for SAR tomography of forested areas. IEEE Trans Geosci Remote Sens, 2013, 51: 5283–5295
4 Lin Y, Hong W, Tan W X, et al. Airborne circular SAR imaging: results at P-band. In: Proceedings of IEEE International Geoscience and Remote Sensing Symposium (IGARSS), Munich, 2012. 5594–5597
5 Shi J, Zhang X L, Xiang G, et al. Signal processing for microwave array imaging: TDC and sparse recovery. IEEE Trans Geosci Remote Sens, 2012, 50: 4584–4598
6 Du L, Wang Y P, Hong W, et al. A three-dimensional range migration algorithm for downward-looking 3-D-SAR with single-transmitting and multiple-receiving linear array antennas. EURASIP J Adv Signal Process, 2010, 2010: 1–15
7 Peng X M, Hong W, Wang Y P, et al. Polar format imaging algorithm with wave-front curvature phase error compensation for airborne DLSLA three-dimensional SAR. IEEE Geosci Remote Sens Lett, 2014, 11: 1036–1040
8 Weib M, Ender J H G. A 3-D imaging radar for small unmanned airplanes-ARTINO. In: Proceedings of European Radar Conference, Paris, 2005. 209–212
9 Peng X M, Wang Y P, Hong W, et al. Airborne downward looking sparse linear array 3-D SAR heterogeneous parallel simulation. Remote Sens, 2013, 5: 5304–5329
10 Wei S J, Zhang X L, Shi J. Linear array sar imaging via compressed sensing. Progress in Electromagn Res, 2011, 117: 299–319
11 Ren X Z, Chen L, Yang J. 3-D imaging algorithm for down-looking MIMO array SAR based on Bayesian compressive sensing. Int J Antenn Propag, 2014, 2014: 612326
12 Li Z, Chen J, Li C S. Spaceborne SIMO-SAR for three-dimensional ionospheric irregularity sounding. IEEE Trans Aero Electron Syst, 2014, 50: 2830–2846
13 Candes E J, Wakin M B. An Introduction to Compressive Sampling. IEEE Signal Process Mag, 2008, 25: 21–30
14 Fannjiang A, Tseng H C. Compressive radar with off-grid targets: a perturbation approach. Inverse Problems, 2013, 29: 054008
15 Chi Y, Scharf L L, Pezeshki A, et al. Sensitivity to basis mismatch in compressed sensing. IEEE Trans Signal Process, 2011, 59: 2182–2195
16 Rao W, Li G, Wang X, et al. Adaptive Sparse Recovery by Parametric Weighted L1 Minimization for ISAR Imaging of Uniformly Rotating Targets. IEEE J Sel Topics Appl Earth Observ Remote Sens, 2013, 6: 942–952
17 He X Y, Liu C C, Liu B, et al. Sparse frequency diverse MIMO radar imaging for off-grid target based on adaptive iterative map. Remote Sens, 2013, 5: 631–647
18 Yan H C, Xu J, Xia X G, et al. Wideband underwater sonar imaging via compressed sensing with scaling effect compensation. Sci China Inf Sci, 2015, 58: 020306

19 Tang G, Bhaskar B N, Shah P, et al. Compressed sensing off the grid. IEEE Trans Inf Theory, 2013, 59: 7465–7490
20 Bhaskar B N, Tang G, Recht B. Atomic norm denoising with applications to line spectral estimation. IEEE Trans Signal Process, 2013, 61: 5987–5999
21 Yang Z, Xie L H. Continuous compressed sensing with a single or multiple measurement vectors. In: Proceedings of IEEE Workshop on Statistical Signal Processing (SSP), Gold Coast, 2014. 288–291
22 Zhang Z, Zhang B C, Jiang C L, et al. Influence factors of sparse microwave imaging radarsystem performance: approaches to waveformdesign and platform motion analysis. Sci China Inf Sci, 2012, 55: 2301–2317
23 Grant M, Boyd S. CVX: Matlab software for disciplined convex programming. Version 2.1. http://cvxr.com/cvx. 2014
24 Daubechies I, Defriese M, de Mol C. An iterative thresholding algorithm for linear inverse problems with a sparsity constraint. Commun Pure Appl Math, 2004, 57: 1413–1457
25 van Trees H L. Optimum Array Processing: Part IV of Detection, Estimation, and Modulation Theory. New York: Wiley, 2002
26 Toh K C, Todd M J, Tütüncü R H. SDPT3 — a MATLAB software package for semidefinite programming, ver 1.3. Optimiz Method Softw, 1999, 11: 545–581